Monthly Notices of the ROYAL ASTRONOMICAL SOCIETY

MNRAS **515,** 543–554 (2022) https://doi.org/10.1093/mnras/stac1802
Advance Access publication 2022 June 30

FAUST VI. VLA1623–2417 B: a new laboratory for astrochemistry around protostars on 50 au scale

C. Codella,[1,2★] A. López-Sepulcre,[2,3] S. Ohashi,[4] C. J. Chandler,[5] M. De Simone,[1,2] L. Podio,[1] C. Ceccarelli,[2] N. Sakai,[4] F. Alves,[6] A. Durán,[7] D. Fedele,[1] L. Loinard,[7,8] S. Mercimek,[1,9] N. Murillo,[4] Y. Zhang,[4] E. Bianchi,[1,2] M. Bouvier,[2] G. Busquet,[10] P. Caselli,[11] F. Dulieu,[12] S. Feng,[13] T. Hanawa,[14] D. Johnstone,[15,16] B. Lefloch,[2] L. T. Maud,[17] G. Moellenbrock,[5] Y. Oya,[18,19] B. Svoboda[5] and S. Yamamoto[18,19]

Affiliations are listed at the end of the paper

Accepted 2022 June 24. Received 2022 June 13; in original form 2022 May 3

ABSTRACT

The ALMA (Atacama Large Millimeter Array) interferometer, with its unprecedented combination of high sensitivity and high angular resolution, allows for (sub-)mm wavelength mapping of protostellar systems at Solar system scales. Astrochemistry has benefitted from imaging interstellar complex organic molecules in these jet–disc systems. Here, we report the first detection of methanol (CH_3OH) and methyl formate ($HCOOCH_3$) emission towards the triple protostellar system VLA1623–2417 A1+A2+B, obtained in the context of the ALMA Large Programme FAUST (Fifty AU STudy of the chemistry in the disc/envelope system of solar-like protostars). Compact methanol emission is detected in lines from E_u = 45 K up to 61 K and 537 K towards components A1 and B, respectively. Large velocity gradient analysis of the CH_3OH lines towards VLA1623–2417 B indicates a size of 0.11–0.34 arcsec (14–45 au), a column density $N_{CH_3OH} = 10^{16}$–10^{17} cm^{-2}, kinetic temperature $\geq$ 170 K, and volume density $\geq 10^8$ cm^{-3}. A local thermodynamic equilibrium approach is used for VLA1623–2417 A1, given the limited E_u range, and yields $T_{rot} \leq 135$ K. The methanol emission around both VLA1623–2417 A1 and B shows velocity gradients along the main axis of each disc. Although the axial geometry of the two discs is similar, the observed velocity gradients are reversed. The CH_3OH spectra from B show two broad (4–5 km s^{-1}) peaks, which are red- and blueshifted by ∼ 6–7 km s^{-1} from the systemic velocity. Assuming a chemically enriched ring within the accretion disc, close to the centrifugal barrier, its radius is calculated to be 33 au. The methanol spectra towards A1 are somewhat narrower (∼ 4 km s^{-1}), implying a radius of 12–24 au.

Key words: astrochemistry – ISM: molecules – stars: formation – Individual object: VLA1623–2417.

1 INTRODUCTION

The Sun-like star-forming process transforms dust and gas within a molecular cloud into a star surrounded by its planetary system (e.g. Andre, Ward-Thompson & Barsony 2000; Frank et al. 2014, and references therein). During each evolutionary phase, matter evolves chemically increasing its complexity (e.g. Ceccarelli et al. 2007; Herbst & van Dishoeck 2009; Caselli & Ceccarelli 2012, and references therein). The earliest protostellar phases are represented by Class 0 and I objects (10^4–10^5 yr) and characterized by three major components: (i) an infalling and rotating envelope, (ii) an accretion disc, rotating along the protostellar equatorial plane, and feeding the star, and (iii) a fast (∼100 km s^{-1}) jet and slower disc wind shedding angular momentum to allow the system to continue accreting mass. In addition, the inner 100 au of the protostellar region is associated with a temperature >100 K, which make dust mantles sublimate and in turn enrich the gas mixture. Additionally, heating via shocks is expected where the infalling material meets the disc, close to the centrifugal barrier (Stahler et al. 1994). As a consequence, chemically enriched rotating rings are predicted and have recently been observed in several objects, starting from the prototypical L1527 (Sakai et al. 2014a,b, 2017; Oya et al. 2016).

One of the breakthrough lessons provided by the ALMA (Atacama Large Millimeter Array) interferometer[1] is that rings and gaps exist in protoplanetary discs around stars younger than 1 Myr (e.g. Sheehan & Eisner 2017; Fedele et al. 2018; Segura-Cox et al. 2020). This indicates that the process of planet formation starts earlier than commonly thought. These findings in turn highlight the importance of studying the chemical content at the Class 0/I stages, especially imaging interstellar complex organic molecules (iCOMs; species with at least six atoms, e.g. CH_3OH), considered the first step towards a true prebiotic chemistry (Herbst & van Dishoeck 2009; Ceccarelli et al. 2017). This is one of the goals of the ALMA Large Program (LP) FAUST[2] (Fifty AU STudy of the chemistry in the disc/envelope system of solar-like protostars), focused on

★ E-mail: claudio.codella@inaf.it

[1] https://www.almaobservatory.org
[2] http://faust-alma.riken.jp

astrochemistry of protostars imaged at the Solar system spatial scale. A full description of the FAUST project is presented by Codella et al. (2021). Key questions investigated are: Do all Sun-like analogues pass through a hot-corino phase, and/or are they associated with chemical enrichment in the external regions (rings) of the accretion disc? FAUST also provides the opportunity to sample the chemistry of star-forming regions in the Southern hemisphere, opening new protostellar laboratories in which to investigate the composition of gas in the regions where planets are going to form.

In this paper, we provide the first survey of iCOM emission from the southern protostellar cluster VLA1623−2417, reporting detection of CH_3OH (methanol) and $HCOOCH_3$ (methyl formate).

1.1 The VLA1623−2417 multiple protostars

One of the best laboratories in which to study the chemical composition around multiple protostars is VLA1623−2417 (hereafter VLA1623), located in Ophiuchus A at a distance of 131 ± 1 pc (Gagné et al. 2018). VLA1623 is a well-known multiple system with two sources labelled A and B (separated by about 1 arcsec, ∼130 au), previously traced from cm to submm (e.g. Andre et al. 1990; Leous et al. 1991; André, Ward-Thompson & Barsony 1993; Looney, Mundy & Welch 2000; Ward-Thompson et al. 2011; Murillo et al. 2018a,b, and references therein). VLA1623 A has been considered one of the prototypical Class 0 objects (André et al. 1993; Murillo et al. 2013). Harris et al. (2018), however, recently showed that source A is actually a binary system composed of two objects, A1 and A2, separated by less than 30 au, and surrounded by a circumbinary disc well detected at 0.9 mm. The nature of source B, on the other hand, is still controversial (Murillo & Lai 2013; Murillo et al. 2013, 2018a,b): (i) it is associated with water masers (Furuya et al. 2003) and it has a spectral energy distribution similar to VLA1623 A (Murillo et al. 2018b), and (ii) it lies outside the A1 + A2 circumbinary disc (see also Hsieh et al. 2020). In addition, Hsieh et al. (2020) suggest the occurrence of SO detected accretion flows on scales larger than 100 au moving towards VLA1623 B.

About 1200 au west of the VLA1623 A1+A2+B triple system, a further object, labelled W, has been revealed (e.g. Harris et al. 2018, and references therein). It has been proposed that VLA1623 W is a shocked cloudlet, part of the large-scale outflow driven by A (e.g. Hara et al. 2021). However, Murillo & Lai (2013), analysing the spectral energy distribution, revealed it as a Class I object (see also Harris et al. 2018). Large-scale outflowing material (e.g. in CO and H_2) originating near the VLA1623 A and B multiple system has been detected along an NW–SE direction (e.g. Andre et al. 1990; Caratti o Garatti et al. 2006, and references therein), though the number of flows as well as the driving sources are yet to be fully understood. Santangelo et al. (2015) imaged a fast jet from VLA1623 B, while Hsieh et al. (2020) analysed VLA1623 in several molecular tracers (CO isotoplogues, SO, DCO^+) with ALMA and reported the occurrence of two cavities at the same position but moving at different velocities, proposing that VLA1623 A and VLA1623 B are driving two molecular outflows on the plane of the sky and on top of each other. More recently, Hara et al. (2021) traced VLA1623 in CO with ALMA observing two outflows along the projected NW–SE direction, but in this case proposing A1 and A2 as the driving sources. Finally, Ohashi et al. (2022), as part of ALMA-FAUST, sampled the 50 au spatial scale using CS, CCH, and HCO^+ and found: (i) a unique, wide, rotating, and low-velocity cavity (with a PA of ∼125°, i.e. NW–SE) opened by A1; (ii) a large-scale (∼2000 au) envelope as well as a circumbinary disc around A1 and A2, also rotating with the same sense of the outflow cavity; and (iii) CS emission tracing the disc around VLA1623 B, which is rotating in the opposite direction with respect to the other components of the system.

Wrapping up, the dust and the molecular content of the VLA1623 cluster previously has been extensively investigated; the missing piece of the puzzle is to understand the molecular complexity around the four protostars within the cluster via an iCOM survey.

2 OBSERVATIONS

The VLA1623 multiple system was observed on 2018 December, 2019 April, and 2020 March with ALMA Band 6 (FAUST Large Program 2018.1.01205.L), using different configurations from 40 to 49 antennas. We observed two frequency ranges: (i) 214.0–219.0 and 229.0–234.0 GHz (Setup 1), and (ii) 242.5–247.5 and 257.2–262.5 GHz (Setup 2). Both Setups 1 and 2 were observed over 12 spectral windows with a bandwidth/frequency resolution of 59 MHz/122 kHz (82 km s^{-1}/0.17–0.20 km s^{-1}) and one with a bandwidth of 1.9 GHz (2640–2798 km s^{-1}). For the latter window, the frequency resolution was 0.5 MHz (0.72 km s^{-1}) for Setup 1, and 1 MHz (1.39 km s^{-1}) for Setup 2. The baselines were between 15 m (B_{min}) and 969 m (B_{max}). The maximum recoverable scale ($\theta_{MRS} \sim 0.6\,\lambda\,B_{min}^{-1}$) is ∼ 40–45 arcsec.

The observations were centred at $\alpha_{J2000} = 16^h26^m26\overset{s}{.}392$, $\delta_{J2000} = -24°24'30\overset{''}{.}178$. The flux was calibrated using the quasars J1427−4206, J1517−2422, and J1626−2951, reaching an absolute flux calibration uncertainty of 10 per cent. The data were self-calibrated using line-free continuum channels. The ALMA calibration pipeline within CASA 5.6.1 (McMullin et al. 2007) was used and we included an additional calibration routine to correct for T_{sys} issues and spectral data normalization.[3] The resulting continuum-subtracted line-cube was cleaned with a Briggs robust parameter of 1. The typical synthesized beams are 0.45 arcsec × 0.36 arcsec (PA = +96°), for Setup 1, and 0.46 arcsec × 0.43 arcsec (PA = −80°), for Setup 2. The typical rms noise is ∼ 1–2 mJy $beam^{-1}$. Self-calibration improved the dynamic range of the continuum images by factors between 3 and 10, depending on the data set and configuration. The final rms noise is as expected for the integration time and bandwidth. The data analysis was performed using the IRAM-GILDAS[4] package.

3 RESULTS

3.1 Continuum emission

Fig. 1 shows the VLA1623 region as observed in dust continuum emission at 1.2 mm. VLA1623 A is well detected, without disentangling the binary components A1 and A2 at the 0.4 arcsec (52 au) angular resolution. The circumbinary disc around A is well traced, in agreement with previous observations (see e.g. Harris et al. 2018). Furthermore, the B and W protostars are also well detected. The J2000 coordinates of the A, B, and W protostars can be obtained from a two-dimensional fitting: A: $16^h26^m26\overset{s}{.}392$, $-24°24'30\overset{''}{.}88$; B: $16^h26^m26\overset{s}{.}307$, $-24°24'30\overset{''}{.}75$; W: $16^h26^m25\overset{s}{.}632$, $-24°24'29\overset{''}{.}66$.

Comparing the present continuum images with those obtained at 0.9 mm in 2016 by Harris et al. (2018) using a higher angular resolution (∼0.2 arcsec; see the zoom-in insets of Fig. 1), proper

[3] https://help.almascience.org/kb/articles/what-errors-could-originate-from-the-correlator-spectral-normalization-and-tsys-calibration; Moellenbrock et al. (in preparation)
[4] http://www.iram.fr/IRAMFR/GILDAS

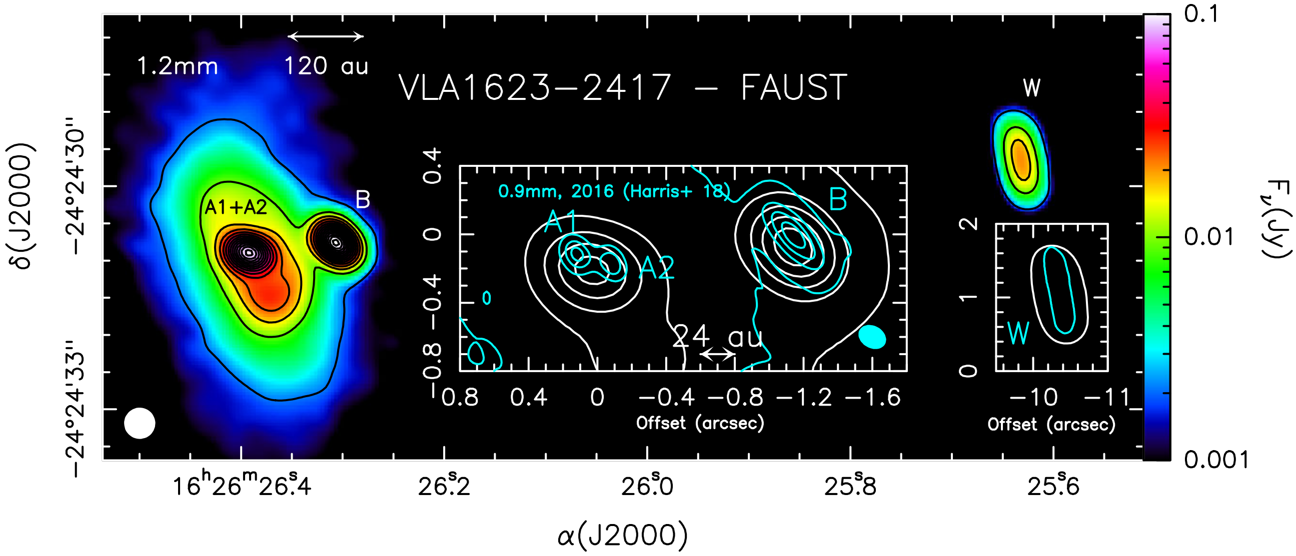

Figure 1. Dust continuum emission at 1.2 mm (colour scale and black contours) from the VLA1623−2717 cluster. First contours and steps are 3σ (2.1 mJy beam^{-1}) and 10σ, respectively. The synthesized beam (bottom left-hand corner) is 0.39 arcsec × 0.36 arcsec (PA = 69°). The A1 and A2 protostars are not disentangled at the present angular resolutions. The B and W protostars are also labelled. The two insets compare the FAUST image (white contours, obtained in 2018) with that obtained with ALMA at 0.9 mm in 2016 (cyan contours) by Harris et al. (2018) with a higher angular resolution (∼ 0.2 arcsec). For sake of clarity, for this comparison, we used a step size of 30σ for the FAUST map. Angular offsets are with respect to the phase centre: α_{J2000} = 16^{h}26^{m}26^{s}.392, δ_{J2000} = −24°24′30.″178.

motion is suggested. For B, the shift in position is $\Delta\alpha = +0.2$ ms and $\Delta\delta = -68$ mas. This shift is also in agreement with that required to align the A1 + A2 positions in the map of Harris et al. (2018) with the A peak in the present map. Further analysis of the continuum observations is beyond the scope of this paper; however, the spatial distribution of the protostars is used to determine the origin of the detected methanol emission reported below.

3.2 Methanol and methyl formate emission

For the first time, the FAUST data set allows imaging methanol (CH_3OH) and methyl formate ($HCOOCH_3$) line emission towards the VLA1623 protostellar system. In addition, upper limits on line emission due to acetaldehyde (CH_3CHO), formamide (NH_2CHO), and dimethyl ether (CH_3OCH_3) are derived (see Table 1).

Previously, methanol was detected through one line observed with the 12 m Kitt Peak single dish by Lindberg, Charnley & Cordiner (2016). Here, we observe methanol emission over eight transitions covering a large range of upper level excitation, E_u, from 45 to 537 K (see Table 1). Only lines with a signal-to-noise ratio (S/N) of at least 5 are considered detected. Fig. 2 shows the spatial distribution of the CH_3OH emission lines (dust continuum emission drawn in magenta): the methanol emission peaks in two very compact regions that are spatially unresolved at the present (∼0.4 arcsec, ∼50 au) angular resolution. Two CH_3OH sources are detected: (i) one associated with the A binary protostar, and revealed only by low-E_u transitions (45–61 K), and (ii) a second, brighter, methanol clump overlapping with the B protostar, and observed up to the E_u = 537 K line.

Fig. 3 reports the CH_3OH spectra extracted at the positions of both the A and B protostars. The CH_3OH line observed with the 12 m antenna by Lindberg et al. (2016) was very narrow (0.44 km s^{-1}), plausibly tracing a large-scale molecular envelope. Here, two different line profiles are observed. The A protostar spectra are well consistent with the systemic velocity of +3.8 km s^{-1} (Narayanan & Logan 2006), and are ∼4 km s^{-1} broad. On the other hand, the B protostar spectra show two spectrally resolved peaks (each ∼4–5 km s^{-1} broad), which are red- and blueshifted by ∼6–7 km s^{-1} with respect to systemic. Thus, the full velocity range covered by CH_3OH is large, from about −12 to +14 km s^{-1}. Note that the $20_{3,\,17}$–$20_{2,\,18}$ (at E_u = 537 K) B protostar spectrum has been smoothed to 8 km s^{-1} in order to reach a higher S/N level; however, it stills shows a profile in agreement with the other CH_3OH spectra.

$HCOOCH_3$ emission has also been revealed: (i) at 233.2 GHz, where two transitions at E_u = 123 K are blended, and (ii) 247.0 GHz, where six transitions with E_u in the 140–177 K range contribute to create an emission peak (see Table 1). Fig. 4 (right-hand panels) shows images of the $HCOOCH_3$ emission, peaking towards the B protostar. No significant emission has been observed towards the A binary protostar. The methyl formate source is spatially unresolved (≤ 50 au). The spectra extracted at the position of the B protostar are reported in Fig. 4 (left-hand panels). The emission covers a wide range of velocities, up to about ±30 km s^{-1} with respect to the systemic velocity. Taking into account that the spectral patterns are associated with multiple transitions, the observed $HCOOCH_3$ profiles are in agreement with the occurrence of blue- and redshifted peaks revealed by the CH_3OH lines.

3.3 Physical properties: LTE and LVG analysis

Given the lack of collisional coefficients for methanol at transitions with rotational number $J \geq 16$ (Rabli & Flower 2010), our approach to deriving physical properties is twofold: (i) a non-LTE (local thermodynamic equilibrium) large velocity gradient (LVG) model, as described by Ceccarelli et al. (2003), for the subsample of CH_3OH transitions associated with collisional rates ($J \leq 15$), and (ii) an LTE model hypothesis using all observed CH_3OH lines.

For the LVG analysis towards the B protostar, we use the CH_3OH–H_2 collisional coefficients computed by Rabli & Flower (2010) for temperatures up to 200 K, and provided by the BASECOL data base (Dubernet et al. 2013). For the computations, we use the five lines

Table 1. Spectral properties and observed velocity integrated intensities of the CH_3OH and $HCOOCH_3$ lines observed towards the position of the VLA1623−2417 A and B sources (see Fig. 1 and Section 3). Upper limits on CH_3CHO, NH_2CHO, and CH_3OCH_3 lines are also reported.

Transition	ν[a] (GHz)	E_u[a] (K)	g_u[a]	$\mathrm{Log_{10}}(A_{ul}/\mathrm{s^{-1}})$[a]	$S\mu^2$[a] (D^2)	F (mJy beam^{-1} km s^{-1}) A	B
CH_3OH $4_{2,3}$–$3_{1,2}$ E	218440.063	45	36	−4.3	13.9	16.3(2.3)	66.5(3.8)
CH_3OH $10_{3,7}$–$11_{2,9}$ E	232945.797	190	84	−4.7	12.1	≤ 9.9	36.7(3.2)
CH_3OH $18_{3,15}$–$17_{4,14}$ A	233795.666	447	148	−4.7	21.9	≤ 9.8	≤ 15.0
CH_3OH $4_{2,3}$–$5_{1,4}$ A	234683.370	61	36	−4.7	4.5	19.9(2.3)	32.8(6.2)[b]
CH_3OH $5_{4,2}$–$6_{3,3}$ E	234689.519	123	44	−5.2	1.9	≤ 9.9	11.1(3.3)[b]
CH_3OH $5_{1,4}$–$4_{1,3}$ A	243915.788	50	44	−4.2	15.5	32.0(2.3)	77.2(3.9)
CH_3OH $20_{3,17}$–$20_{2,18}$ A	246074.605	537	164	−4.1	73.7	≤ 6.2	34.4(2.9)[c]
CH_3OH $19_{3,16}$–$19_{2,17}$ A	246873.301	490	156	−4.1	73.7	≤ 7.3	35.5(3.2)
CH_3OH $16_{2,15}$–$15_{3,13}$ E	247161.950	338	132	−4.6	19.3	≤ 8.3	39.4(3.2)
CH_3OH $4_{2,2}$–$5_{1,5}$ A	247228.587	61	36	−4.7	4.3	16.8(2.8)	37.2(4.8)
CH_3OH $18_{3,15}$–$18_{2,16}$ A	247610.918	447	148	−4.1	69.4	≤ 9.5	35.2(3.8)
CH_3OH $12_{6,7}$–$13_{5,8}$ E	261704.409	360	100	−4.8	8.5	≤ 12.3	≤ 20.4
CH_3CHO $11_{1,10}$–$10_{1,9}$ E	216581.930	65	46	−3.5	69.0	≤ 8.0	≤ 9.8
NH_2CHO $12_{0,12}$–$11_{0,11}$	247390.719	78	25	−3.0	156.3	≤ 9.9	≤ 12.8
NH_2CHO $12_{2,10}$–$11_{2,9}$	260189.090	92	25	−2.9	152.6	≤ 14.8	≤ 21.6
CH_3OCH_3 $18_{5,13}$–$18_{4,14}$ AE	257911.036	191	74	−4.1	32.5	≤ 13.5[d]	≤ 13.5[d]
CH_3OCH_3 $18_{5,13}$–$18_{4,14}$ EA	257911.175	191	148	−4.1	64.9		
CH_3OCH_3 $18_{5,13}$–$18_{4,14}$ EE	257913.312	191	592	−4.1	259.7		
CH_3OCH_3 $18_{5,13}$–$18_{4,14}$ AA	257915.519	191	222	−4.1	57.4		
CH_3OCH_3 $14_{1,14}$–$13_{20,13}$ EA	258548.819	93	116	−3.9	113.2	≤ 15.2[e]	≤ 22.3[e]
CH_3OCH_3 $14_{1,14}$–$13_{20,13}$ AE	258548.819	93	174	−3.9	75.5		
CH_3OCH_3 $14_{1,14}$–$13_{20,13}$ EE	258549.063	93	464	−3.9	301.9		
CH_3OCH_3 $14_{1,14}$–$13_{20,13}$ AA	258549.308	93	290	−3.9	188.7		
$HCOOCH_3$ $19_{17,2}$–$18_{17,1}$ E	233212.773	123	78	−3.7	48.0	≤ 18.2[f]	36.9(6.2)[f]
$HCOOCH_3$ $19_{4,16}$–$18_{4,15}$ A	233226.788	123	78	−3.7	48.0		
$HCOOCH_3$ $19_{4,14}$–$18_{4,13}$ E	233753.960	114	74	−3.7	45.8	≤ 10.8	≤ 15.2
$HCOOCH_3$ $19_{4,14}$–$18_{4,14}$ A	233777.521	114	74	−3.7	45.8	≤ 10.8	≤ 13.8
$HCOOCH_3$ $20_{10,10}$–$19_{0,9}$ E	246600.012	190	82	−3.8	40.0	≤ 12.2	≤ 15.2
$HCOOCH_3$ $20_{10,11}$–$19_{10,10}$ A	246613.392	190	82	−3.8	40.0	≤ 12.1[g]	≤ 15.3[g]
$HCOOCH_3$ $20_{10,10}$–$19_{10,9}$ A	246613.392	190	82	−3.8	40.0		
$HCOOCH_3$ $20_{9,11}$–$19_{9,10}$ E	247040.650	177	82	−3.7	42.5	≤ 22.8[h]	90.0(5.3)[h]
$HCOOCH_3$ $20_{10,11}$–$19_{10,10}$ A	247044.146	140	86	−3.7	54.0		
$HCOOCH_3$ $21_{3,19}$–$20_{3,18}$ E	247053.453	140	86	−3.7	54.0		
$HCOOCH_3$ $20_{9,11}$–$19_{9,10}$ E	247057.259	178	82	−3.7	42.5		
$HCOOCH_3$ $20_{9,11}$–$19_{9,10}$ A	247057.737	178	82	−3.7	42.5		
$HCOOCH_3$ $20_{9,12}$–$19_{9,11}$ E	247063.662	177	82	−3.7	42.5		
$HCOOCH_3$ $21_{7,14}$–$20_{7,13}$ E	261715.518	170	86	−3.6	48.7	≤ 16.7	≤ 21.3

[a]Spectroscopic parameters of CH_3OH, NH_2CHO, and CH_3OCH_3 are from Xu & Lovas (1997), Xu et al. (2008), Motiyenko et al. (2012), and Endres et al. (2009), retrieved from the CDMS data base (Müller et al. 2005). For CH_3CHO and $HCOOCH_3$, we refer to data by Kleiner, Lovas & Godefroid (1996) and Ilyushin, Kryvda & Alekseev (2009), retrieved from the JPL data base (Pickett et al. 1998).

[b]Given the blending of the $5_{4,2}$–$6_{3,3}$ E redshifted emission with the blueshifted peak of the CH_3OH $4_{2,3}$–$5_{1,4}$ A profile, the measurements should be considered as lower limits.

[c]All the spectra have been resampled to a velocity resolution of 1.2 km s^{-1}, with the exception of the weak $CH_3OH(18_{3,15}$–$18_{2,16})$ A and $HCOOCH_3(19_{17,2}$–$18_{17,1})$ A emission, smoothed to 8 and 6 km s^{-1}, respectively. The upper limits refer to the 3σ values. CH_3OH: For source A, the velocity interval is −3, +7 km s^{-1}. For source B, the methanol emission has been integrated on the −11, +13 km s^{-1} interval for all the lines but the $18_{3,15}$–$18_{2,16}$ A one, for which we adopted −16, +19 km s^{-1}. $HCOOCH_3$: The emission has been integrated from −22 to +32 km s^{-1} and in the −20, +29 km s^{-1} range for $19_{17,2}$–$18_{17,1}$ E and $21_{3,19}$–$20_{3,18}$ E, respectively. [d]to [h] Blended lines of the same species.

with E_u in the 45–190 K range, and assume an H_2 ortho-to-para ratio equal to 3. We run grids of models varying the kinetic temperature (T_{kin}) from 50 to 200 K, the volume density (n_{H_2}) from 10^7 to 10^{11} cm^{-3}, and the methanol column density (N_{CH_3OH}) from 10^{15} to 10^{18} cm^{-2}. We then simultaneously fit the measured CH_3OH A and CH_3OH E line intensities via comparison with those simulated by the LVG model, leaving N_{CH_3OH}, n_{H_2}, T_{kin}, and the emitting size θ as free parameters. The errors on the observed line intensities have been obtained by propagating the spectral rms with the uncertainties due to calibration (10 per cent). The limited number of methanol lines and the fact that four lines out of five are in the narrow E_u = 45–61 K range make this analysis challenging. However, several useful constraints are obtained. The lowest χ_r^2 values (∼2) are obtained for sizes between 0.11 arcsec (14 au) and 0.34 arcsec (45 au), in agreement

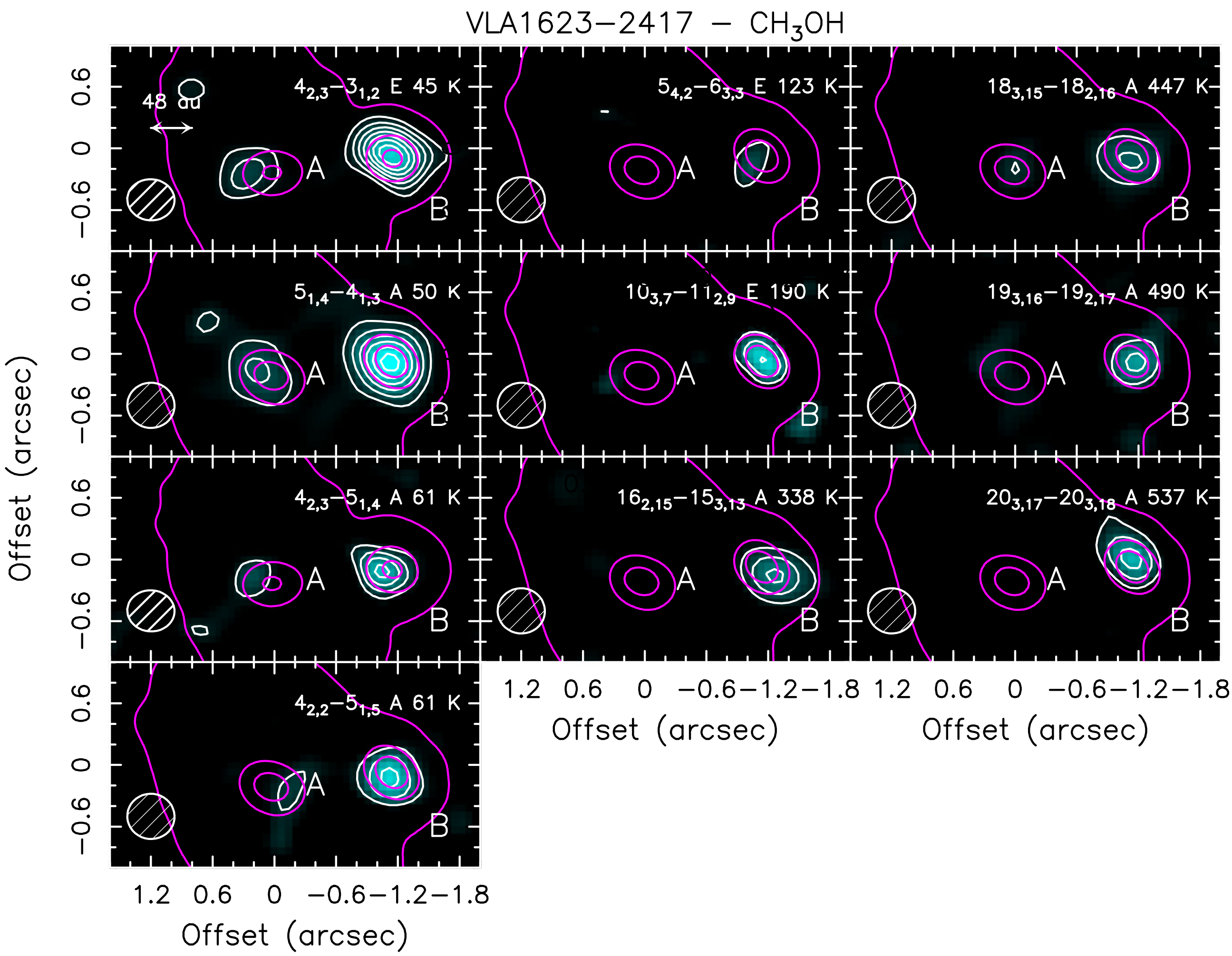

Figure 2. The VLA1623 cluster as imaged using the CH_3OH lines (white contours) reported in Table 1. In magenta we show selected contours from the (Setup 1 and Setup 2, depending on the line) continuum emission maps, drawn to pinpoint the location of the A and B protostars. Angular offsets are with respect to the phase centre: $\alpha_{J2000} = 16^h26^m26\overset{s}{.}392$, $\delta_{J2000} = -24°24'30\overset{''}{.}178$. Transitions and upper level energies are reported. The emission has been integrated from −11 to +14 km s^{-1} for all the lines except the $20_{3,\,17}$–$20_{2,\,18}$ A line, which is integrated in the −16, +24 km s^{-1} range, and the (blended, see Fig. 3) $5_{4,\,2}$–$6_{3,\,3}$ E line, which is integrated in the −11, +9 km s^{-1} range. First white contours and steps are 3σ and 2σ, respectively. The σ values are 6 mJy km s^{-1} beam^{-1} ($5_{1,\,4}$–$4_{1,\,3}$, $16_{2,\,15}$–$15_{3,\,13}$, $18_{3,\,15}$–$18_{2,\,16}$, $19_{3,\,16}$–$19_{2,\,17}$), 4 mJy km s^{-1} beam^{-1} ($4_{2,\,3}$–$3_{1,\,2}$, $5_{4,\,2}$–$6_{3,\,3}$, $20_{3,\,17}$–$20_{2,\,18}$), and 5 mJy km s^{-1} beam^{-1} ($4_{2,\,2}$–$5_{1,\,5}$, $10_{3,\,7}$–$11_{2,\,9}$). The synthesized beams (the hatched ellipse in the bottom left-hand corner) are 0.45 arcsec × 0.36 arcsec (PA = +96°) and 0.46 arcsec × 0.43 arcsec (PA = −80°) for Setup 1 and Setup 2, respectively.

with the observed unresolved spatial distributions. The methanol line opacities are predicted to be less than 0.1 and the A + E methanol column density N_{CH_3OH} ranges in the 10^{16}–10^{17} cm^{-2} interval. Fig. 5 shows the χ_r^2 contour plot in the T_{kin}–n_{H_2} plane obtained for a representative case (0.28 arcsec, 2×10^{16} cm^{-2}). In addition, Fig. 5 shows the ratio between observations and model predictions for the CH_3OH A (circles) and E (stars) line intensity as a function of the upper level energy of the lines. The 1σ (blue; 30 per cent to exceeding χ_r^2) contour delimits the n_{H_2}–T_{kin} degeneracy: $n_{H_2} \geq 10^8$ cm^{-3} and $T_{kin} \geq 170$ K (see Table 2). These physical conditions are indeed reasonable for the inner 50 au region around protostars as sampled by methanol (e.g. Bianchi et al. 2020, and references therein).

Assuming an LTE population and optically thin lines (supported by the LVG analysis), we also construct rotational diagrams (RDs). For a given molecule, the relative population distribution of all the energy levels is described by a Boltzmann temperature, that is the rotational temperature T_{rot}. The critical densities of the CH_3OH lines for temperatures larger than 50 K, when applicable (Rabli & Flower 2010), are $\sim 10^5$–10^6 cm^{-3}. The volume densities found for the LVG analysis of methanol are indeed larger than 10^8 cm^{-3}, supporting the fact that the LTE condition is satisfied. Fig. 6 shows the RD of CH_3OH, derived for both protostars A and B (see also Table 3). Upper limits are reported with grey arrows, as well as the lower limit derived for the $4_{2,\,3}$–$5_{1,\,4}$ A flux towards VLA1623 B (see Section 4.2). For source B, the fit provides a column density N_{tot} = $2.2 \pm 0.2 \times 10^{15}$ cm^{-2} (not corrected for the filling factor), and a rotational temperature of 177 ± 8 K. These estimates are in very good agreement with the LVG results confirming that LTE and optically thin conditions are satisfied. In addition, the RD fit for source B (χ_r^2 = 4) shows that even the very high E_u (338–537 K) lines do not require additional excitation mechanisms different from collisions, such as an infrared radiation field from the protostar. For source A, the E_u range sampled by the four detected lines is too small to obtain a proper free fit. However, we used the upper limits on the high-excitation lines to constrain the rotational temperature. If we assume that the 3σ upper limits on the lines with E_u larger than 300 K are real

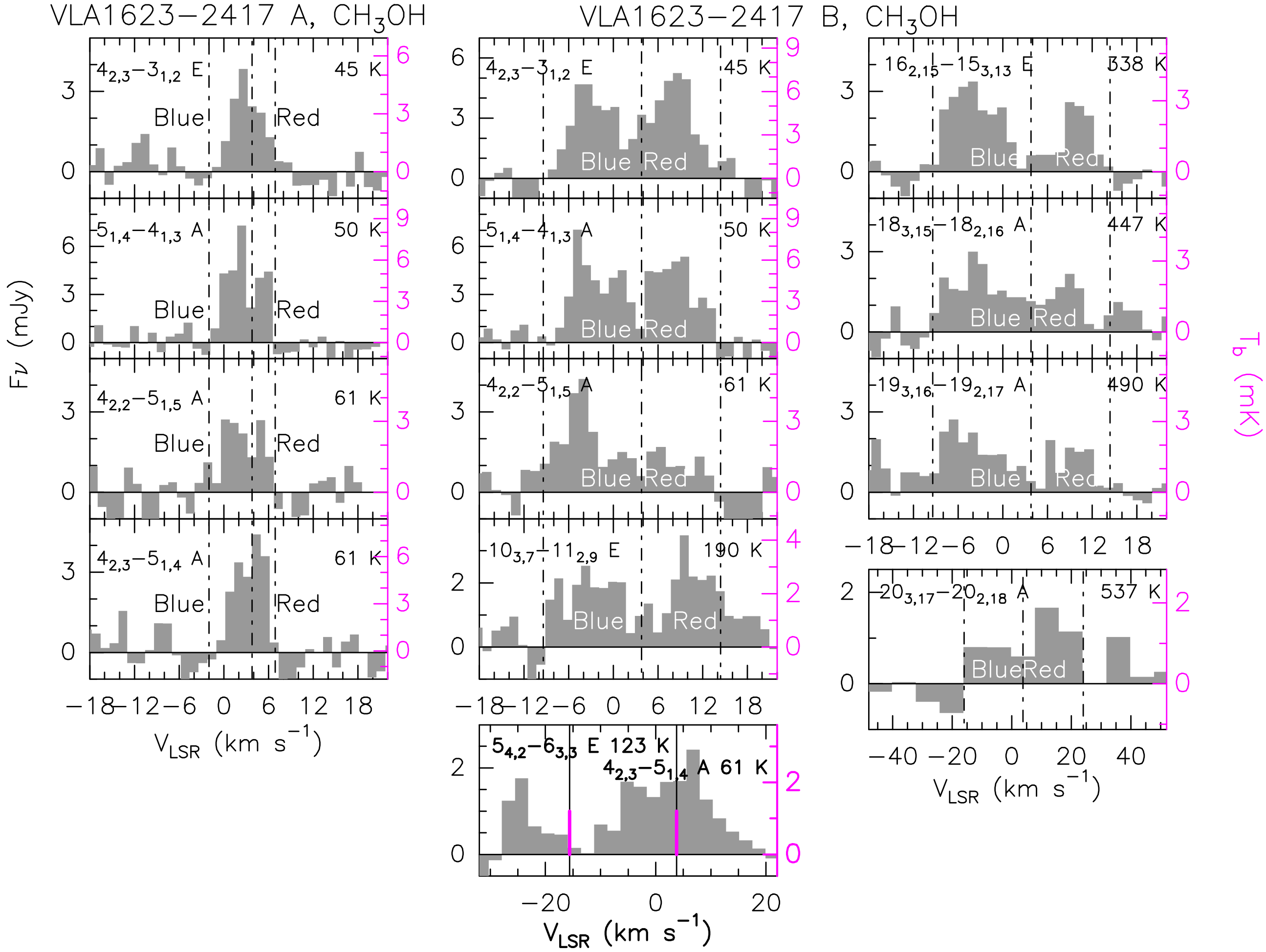

Figure 3. Observed CH_3OH line spectra (in both F_ν and T_B scales) at the positions of the VLA1623 A binary protostar (left-hand panels) and B protostar (middle and right-hand panels). Transitions and upper level energies are reported. The vertical dashed lines mark: the systemic local standard of rest (LSR) velocity (+3.8 km s^{-1}; Narayanan & Logan 2006), as well as the velocity ranges of the red- and blueshifted emission used to derive velocity integrated maps (see Table 1 and Fig. 2) and maps of the blue- and redshifted emissions (see Fig. 7). Note that the $4_{2,3}$–$5_{1,4}$ A and $5_{4,2}$–$6_{3,3}$ spectra towards B (smoothed to a spectral resolution of 2.4 km s^{-1} to increase the S/N) are blended: The continuous black and magenta lines show the differences between their rest frequencies (in the velocity scale).

detecitons, we obtain T_{rot} = 135 K. The real rotational temperature has to be lower, given these upper limits for the brightness of the lines. If T_{rot} = 135 K, then N_{tot} is $\sim 6 \times 10^{14}$ cm^{-2}. The column density decreases for lower temperature, e.g. down to $\sim 6 \times 10^{13}$ cm^{-2}, if the rotational temperature is 50 K.

Methyl formate emission has been detected through two spectral patterns containing contributions by different transitions and, in one case, different upper level excitations. In order to take into account the multiple transitions, we assume (i) the same line profiles for all transitions, and (ii) the same rotational temperature obtained from the LTE analysis of methanol. More specifically, the total column density is obtained by fitting the line profiles using the GILDAS–WEEDS tool (Maret et al. 2011), finding $N_{HCOOCH_3} = 8 \times 10^{14}$ and $\leq$ 2–3 $\times 10^{14}$ cm^{-2} (not corrected for filling factor effects) for sources B and A, respectively (see Table 3). Finally, transitions of acetaldehyde (CH_3OCH), formamide (NH_2CHO), and dimethyl ether (CH_3OCH_3) fall inside the observed frequency windows, but no emission over 3σ has been found. Table 3 reports the upper limits on the total column density derived for these species using the same methodology adopted for methyl formate: $N_{CH_3CHO} \leq$ 1–3 $\times 10^{14}$ cm^{-2}, $N_{NH_2CHO} \leq$ 0.1–5 $\times 10^{14}$ cm^{-2}, and $N_{CH_3OCH_3} \leq$ 4–9 $\times 10^{14}$ cm^{-2}. These values are not corrected for the filling factors. If we take as representative the LVG analysis of methanol emission towards VLA1623 B, the filling factor ranges from 7×10^{-2} to 0.41.

In summary, the compact CH_3OH and $HCOOCH_3$ emission, and the high rotational temperatures are consistent with thermal sublimation of the methanol molecules from icy mantles at temperatures higher than 100 K, namely the classical definition of a hot corino (Ceccarelli et al. 2003). This conclusion specifically applies to source B, while the origin of methanol emission in source A is less constrained. These findings are further discussed in Section 4.1, taking into account the observed kinematics.

4 DISCUSSION

4.1 Kinematics: on the origin of chemical enriched gas in VLA1623 A + B

Fig. 7 shows the red- and blueshifted CH_3OH emission observed towards the VLA1623 A (left-hand panels) and B (middle and right-hand panels) protostars. The emission is integrated between −11 km s^{-1} (–2 km s^{-1}) and +14 km s^{-1} (+7 km s^{-1}) for VLA1623

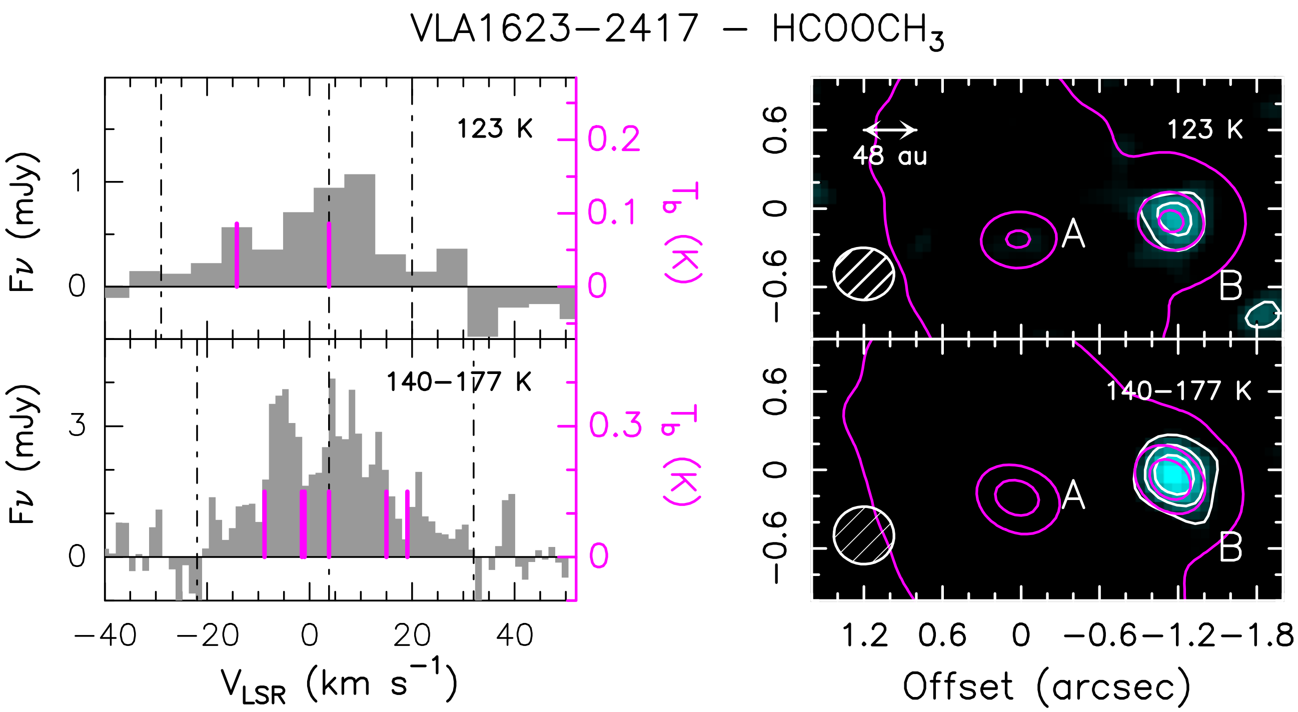

Figure 4. Right-hand panels: the VLA1623 cluster as imaged using the $HCOOCH_3$ lines (white contours) reported in Table 1. In magenta we report selected contours from the (Setup 1 and Setup 2, depending on the line) continuum emission drawn to pinpoint the A and B protostar position. Angular offsets are with respect to the phase centre: $\alpha_{J2000} = 16^h26^m26\overset{s}{.}392$, $\delta_{J2000} = -24°24'30\overset{''}{.}178$. The emission maps are due to several transitions (see Table 1), blended at the present spectral resolution. The emission has been integrated from −22 to +32 km s^{-1} (covering two transitions with E_u = 123 K, upper) and in the −20, +29 km s^{-1} range (covering six transitions with E_u between 140 and 177 K, lower). First contours and steps are 3σ and 2σ, respectively. The σ values are 6 mJy km s^{-1} beam^{-1} (upper) and 8 mJy km s^{-1} beam^{-1} (lower). The synthesized beams (the hatched ellipse in the bottom left-hand corner) are 0.45 arcsec × 0.36 arcsec (PA = +96°) and 0.46 arcsec × 0.43 arcsec (PA = −80°) for Setup 1 and Setup 2, respectively. Left-hand panels: observed $HCOOCH_3$ line spectra (in both F_ν and T_B scales) at the positions of the B protostar. The vertical dashed line at +3.8 km s^{-1} marks the systemic LSR velocity (Narayanan & Logan 2006). Other dashed lines are drawn to show the velocity range used to obtain the $HCOOCH_3$ spatial distributions. The spectra are centred at the frequency of the $19_{17,\,2}$–$18_{17,\,1}$ E (upper) and $21_{3,\,19}$–$20_{3,\,18}$ E (lower), respectively. Magenta lines indicate the shift in velocity of the other $HCOOCH_3$ lines falling in the observed spectral pattern.

B (A) for all the lines except $20_{3,\,17}$–$20_{2,\,18}$ A, which is integrated in the −16, +24 km s^{-1} range towards VLA1623 B. At high velocities, we clearly separate spatially both the red- and blueshifted regions. Velocity gradients are revealed. More specifically, all the methanol lines around VLA1623 B show a redshifted peak towards NE (with respect to the continuum peak) and a blueshifted peak towards SW. This velocity gradient is along the main axis of the disc as traced by continuum (see e.g. the high-angular-resolution map by Harris et al. 2018, reported in Fig. 1). The same velocity gradient, with the same axis and the same velocity spread, has been recently discovered, in the FAUST context, by Ohashi et al. (2022), using CS(5–4) emission.

What is the origin of this chemically enriched gas? The present data must be interpreted with caution. Fig. 8 shows the position–velocity (PV) diagram of the $CH_3OH(4_{2,\,3}$–$3_{1,\,2})$ E emission (representative of the line sample) for VLA1623 B. The PV has been derived along the direction of the disc equatorial plane as inferred from the continuum map of Harris et al. (2018). Fig. 8 reveals the rotation pattern, indicating also a lack of emission (plausibly due to absorption) at the low-velocity (∼ 2–3 km s^{-1}, see also the corresponding spectrum in Fig. 3) blueshifted emission close to the protostar. A detailed modelling is hampered by the spatial resolution (the beam size across the disc axis is 0.41 arcsec, 53 au) of the map. One possibility is that the rotating methanol emission is tracing the inner portion of the envelope, where the temperature is high enough to thermally evaporate the dust mantles, consistent with the classical hot-corino scenario (Ceccarelli et al. 2003). Another intriguing possibility is that CH_3OH is associated with the protostellar disc, more specifically with the ring-like region where the infalling–rotating envelope gas meets the accretion disc and the gas sheds angular momentum in order to continue its trip to the protostar. In this environment, low-velocity (∼1 km s^{-1}) accretion shocks are expected with the consequent sputtering of dust mantle products into the gas phase. The prototypical protostar where this effect has been revealed is L1527 (Sakai et al. 2014a,b). According to the high-angular-resolution continuum measurements from Harris et al. (2018), the VLA1623 B disc inclination derived from the ratio between the observed minor and major axes is 74°. The protostellar mass is 1.7 $M_\odot$ (Ohashi et al. 2022, and references therein), and the two CH_3OH peaks are located at ± 6–7 km s^{-1} with respect to the systemic velocity. If we assume methanol is tracing an inclined Keplerian disc, the bulk of the emission would arise at a radius of 33 au. Noticeably, this distance is comparable with both the disc size imaged in the continuum by Harris et al. (2018) and the methanol-emitting size derived by the present LVG analysis (14–45 au).

Similar instructive constraints can be derived for VLA1623 A. The maps shown in Fig. 7 clearly indicate that: (i) CH_3OH is also rotating in the NE–SW direction, but with the opposite sense compared to VLA1623 B (as also noted by Ohashi et al. 2022, using CS), and (ii) even though unresolved, it is possible to note that the methanol emission is shifted with respect to the continuum peak towards the

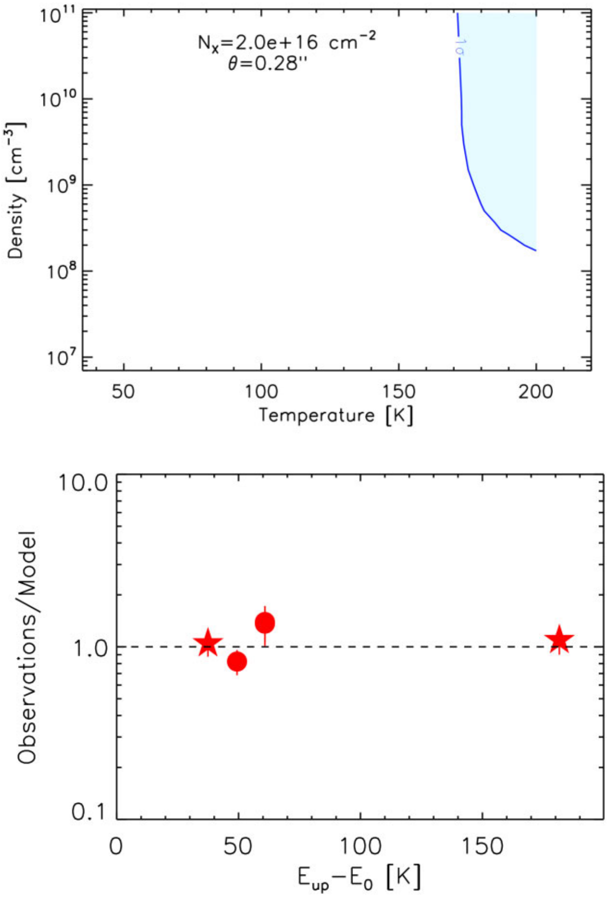

Figure 5. Upper panel: density–temperature contour plot of $\chi_r^2 = 2$, obtained considering the non-LTE LVG model and the observed intensity of all the A and E CH_3OH emission lines detected towards VLA1623 B. The best-fitting case (see text) with size = 0.28 arcsec and N_{CH_3OH} = 2 × 10^{16} cm^{-2} is shown. The 1σ (blue; 30 per cent to exceeding χ_r^2) confidence level delimits the n_{H_2}–T_{kin} values: $n_{H_2} \geq 10^8$ cm^{-3} and $T_{kin} \geq 170$ K. Lower panel: ratio between observations and model predictions of the CH_3OH A (circles) and E (stars) line intensity as a function of the upper level energy of the lines. The ratios are less than 2 for all the five methanol lines (two of them with E_u = 61 K).

Table 2. 1σ confidence level (range) from the non-LTE LVG analysis of the CH_3OH lines towards VLA1623 B.

Size (arcsec)	Size (au)	N_{tot} (cm^{-2})	T_{kin} (K)	n_{H_2} (cm^{-3})
11–34	14–45	10^{16}–10^{17}	$\geq$ 170	$\geq 10^8$

west, where A1 lies. In other words, out of the coeval A1 + A2 binary, only A1 appears to be associated with a hot corino. This chemical differentiation has been indeed found in the (sub-)mm spectral window for several binaries across different star-forming regions (Taquet et al. 2015; De Simone et al. 2017; Belloche et al. 2020; Bianchi et al. 2020; Yang et al. 2021; Bouvier et al. 2022, and references therein). Is this a real chemical differentiation, possibly related to colder conditions, or is it a signature of dust opacity playing a major role at (sub-)mm wavelengths? The latter possibility was explored by De Simone et al. (2020) for the archetypical NGC 1333–IRAS4 A1 + A2 binary system, in Perseus, where according to ALMA only A2 is associated with iCOMs (López-Sepulcre et al.

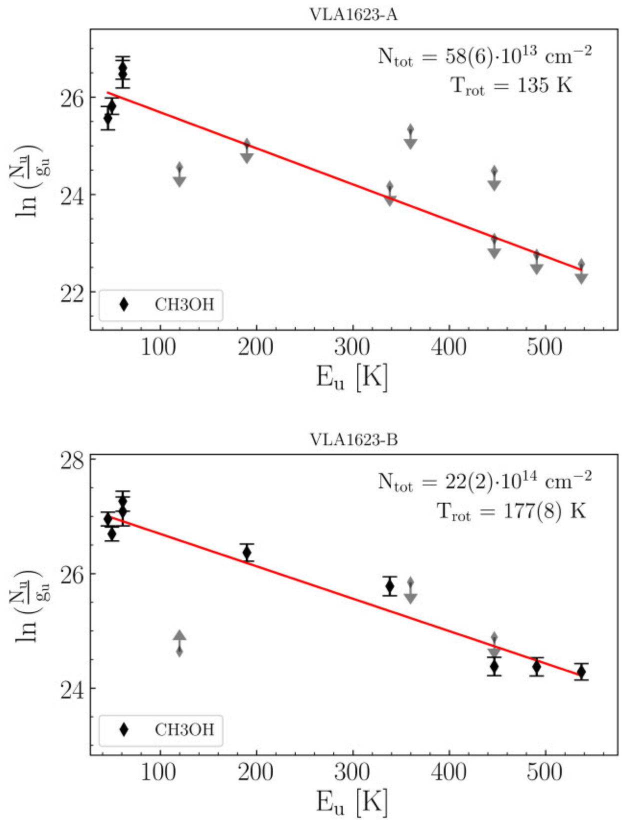

Figure 6. RDs for CH_3OH derived using the emission lines observed towards the continuum peaks associated with VLA1623 A and VLA1623 B (see Fig. 3). The parameters N_u, g_u, and E_{up} are, respectively, the column density, the degeneracy, and the energy (with respect to the ground state of each symmetry) of the upper level. The derived values of the rotational temperature are reported in the panels. No filling factor correction has been applied. Upper limits are reported with grey arrows. Also the lower limit derived for the $4_{2,3}$–$5_{1,4}$ A flux towards VLA1623 B. Note that for VLA1623 A we report the fit done using the upper limits as detections: This implies that the rotation temperature of 135 K is an upper limit (see text).

Table 3. Results of the LTE RD analysis of the iCOM emission observed towards VLA1623 A and VLA1623 B. These values are not corrected for the filling factor derived for CH_3OH in VLA1623 B, which ranges from 7 × 10^{-2} to 0.41 (see text).

Species	VLA1623 A T_{rot} (K)	VLA1623 A N_{tot} (cm^{-2})	VLA1623 B T_{rot} (K)	VLA1623 B N_{tot} (cm^{-2})
CH_3OH	50–135[a]	0.6–6 × 10^{14}	177(8)	22(2) × 10^{14}
$HCOOCH_3$	50–135[b]	$\leq$ 2–3 × 10^{14}	177[b]	8 × 10^{14}
CH_3CHO	50–135[b]	$\leq$ 1–3 × 10^{14}	177[b]	$\leq$ 3 × 10^{14}
NH_2CHO	50–135[b]	$\leq$ 0.3–5 × 10^{14}	177[b]	$\leq$ 10 × 10^{13}
CH_3OCH_3	50–135[b]	$\leq$ 4–6 × 10^{14}	177[b]	$\leq$ 9 × 10^{14}

[a]The upper limit of the range is constrained by the LTE analysis, while the lower end has been assumed.
[b]Assumed, as derived by the methanol LTE analysis. Upper limits refer to 3σ.

2017). De Simone et al. (2020) found that, observing with the JVLA (Jansky Very Large Array) at cm wavelengths, where dust opacity is negligible, A1 is also revealed as a hot corino. The high dust opacity in the (sub-)mm hampers the detection of iCOMs around NGC 1333–

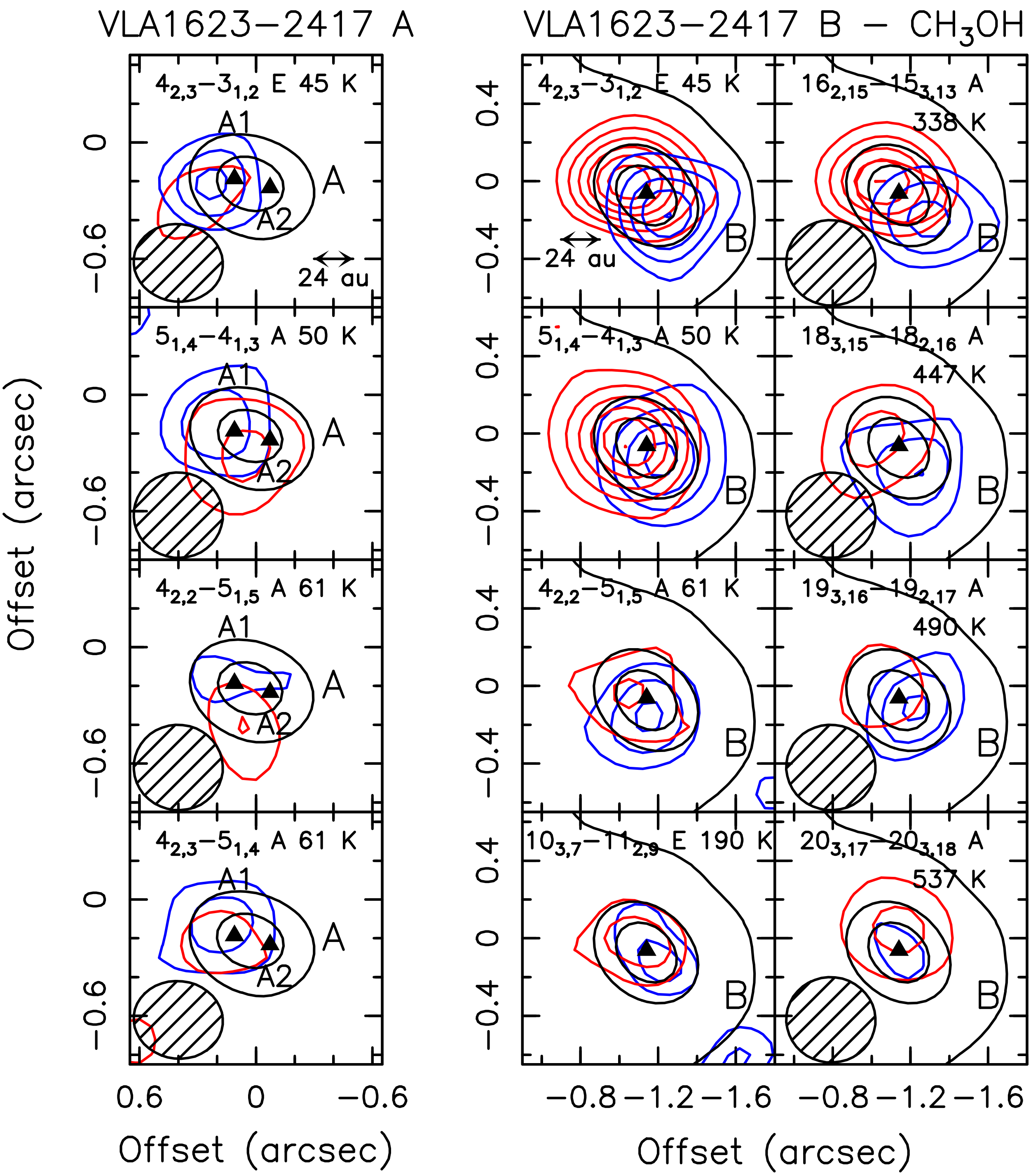

Figure 7. Plot of the red- and blueshifted CH_3OH emission (see Table 1) observed towards VLA1623−2717 A (left-hand panels), and B (middle and right-hand panels) protostars. Transitions and upper level energies are reported. The systemic velocity is +3.8 km s^{-1} (Narayanan & Logan 2006). The emission has been integrated between −11 km s^{-1} (–2 km s^{-1}) and +14 km s^{-1} (+7 km s^{-1}) for VLA1623−2717 B (A) for all the lines except the $20_{3,\,17}$–$20_{2,\,18}$ A line towards VLA1623−2717 B, which is integrated over the −16, +24 km s^{-1} range. Angular offsets are with respect to the phase centre. In black we report selected contours from the continuum emission (Setup 1 and Setup 2) maps, drawn to pinpoint the protostar positions. Black triangles indicate the position of VLA1623−2717 A1, A2, and B as imaged in continuum emission by Harris et al. (2018), obtained with a 0.2 arcsec beam and spatially shifted taking into account the proper motion to allow for a proper comparison with the present methanol images (see text). First contour and steps are 3σ (mJy km s^{-1} beam^{-1}) and 2σ, respectively. The σ values are 3 mJy km s^{-1} beam^{-1} for all the emission maps except $4_{2,\,3}$–$3_{1,\,2}$, $4_{2,\,3}$–$5_{1,\,4}$, and $4_{2,\,2}$–$5_{1,\,5}$ (2 mJy km s^{-1} beam^{-1}), and $5_{1,\,4}$–$4_{1,\,3}$, $10_{3,\,7}$–$11_{2,\,9}$, and $16_{2,\,15}$–$15_{3,\,13}$ (4 mJy km s^{-1} beam^{-1}). The synthesized beams (the hatched ellipse in the bottom left-hand corner) are 0.45 arcsec × 0.36 arcsec (PA = +96°) and 0.46 arcsec × 0.43 arcsec (PA = –80°) for Setup 1 and Setup 2, respectively.

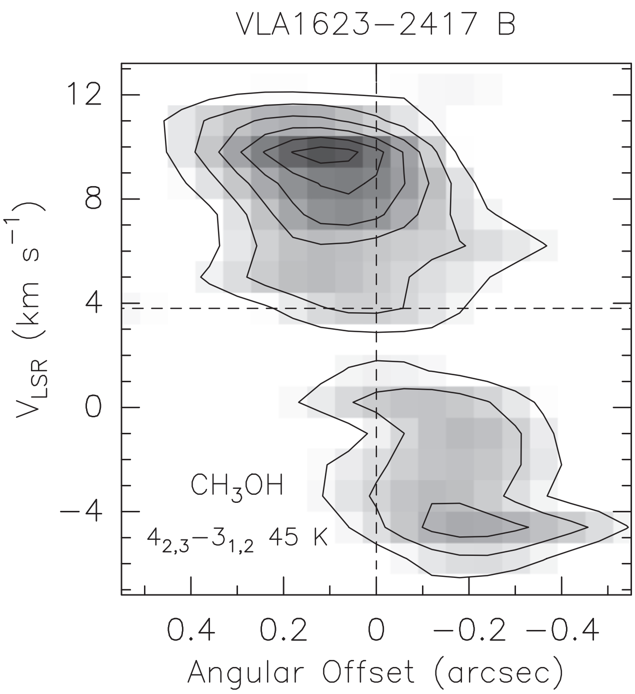

Figure 8. PV cut (beam averaged) of $CH_3OH(4_{2,3}–3_{1,2})$ E along the NE–SW disc around VLA1623 B (Harris et al. 2018). Contour levels range from 3σ by steps of 2σ (128 mK). Dashed lines mark the position of the B protostar and the systemic velocity (+3.8 km s^{-1}; Narayanan & Logan 2006). The angular resolution along the disc axis is 0.41 arcsec, while the spectral resolution is 1.2 km s^{-1}.

IRAS4 A1. Observations at low frequencies will be necessary to provide the final answer on the chemical richness of VLA1623 A2.

Considering further VLA1623 A1, the spectral linewidth is narrower than for VLA1623 B. Using the continuum fit by Harris et al. (2018), for the A1 disc, we derive an inclination angle of 47°. The mass of the A1 protostar is challenging to constrain, however. From line and continuum analysis, the total A1 + A2 mass ranges from 0.2 to 0.4 $M_\odot$ (Murillo et al. 2013; Harris et al. 2018; Ohashi et al. 2022). Assuming for A1 a mass of 0.1–0.2 $M_\odot$, the disc inclination, and that the methanol emission is coming on average from ±2 km s^{-1} with respect to the envelope velocity, we derive a radius of 12–24 au. Again, this size in agreement with ∼ 14–21 au disc derived by Harris et al. (2018) from the A1 continuum.

4.2 Complex organics around VLA1623−2417 B

The detection of CH_3OH and $HCOOCH_3$ towards VLA1623 B opens a new laboratory in which to study the chemical complexity around protostars on Solar system scales. Assuming that both species are emitted from the same region, the $HCOOCH_3/CH_3OH$ abundance ratio, derived from the column densities (not corrected for the filling factor, Table 3), is ∼ 0.4. This value is within the range found in the literature for hot corinos associated with Class 0 or I objects, as imaged by interferometers. If we consider the ALMA-PILS, IRAM-CALYPSO, ALMA-FAUST, and ALMA-PEACHES, a relatively large spread is revealed, from a few 10^{-2} to values close to unity (Jørgensen et al. 2016, 2018; Belloche et al. 2020; Bianchi et al. 2020; Manigand et al. 2020; Yang et al. 2021).

Given that the VLA1623 B disc is close to edge-on (Harris et al. 2018), the present CH_3OH maps resemble the Orion HH212-mm protostellar disc previously observed with ALMA at the same spatial scale, i.e. a velocity gradient of gas enriched in iCOMs around the disc (e.g. Codella et al. 2018, and references therein). HH212-mm is very bright in both dust and line emission, and a large number of iCOMs have been imaged. The $HCOOCH_3/CH_3OH$ abundance ratio, in the HH212-mm case, is 2 × 10^{-2} (Lee et al. 2019). When observed at higher spatial resolution, down to 10 au (Lee et al. 2017a,b,c, 2019), HH212-mm discloses the region traced by iCOMs: two rotating rings at a radius of ∼40 au associated with the outer surface layers of the disc. The layers lie above and below the equatorial plane by about 40 au. In the plane, (sub-)mm emission from the dust is optically thick and no iCOM emission is detected, plausibly due to opacity effects. As with HH212, two scenarios are possible for VLA1623 B: (i) iCOMs delimit the accretion shock, similarly to what proposed for L1527, or (ii) they arise from portions of the flared disc illuminated directly by the protostar. VLA1623 B offers an excellent opportunity to attack this question given that ALMA can reach spatial scales of ∼3 au, due to the VLA1623 system being closer (∼130 pc) to the Sun compared with Orion (∼400 pc).

5 SUMMARY AND CONCLUSIONS

The FAUST ALMA Large Program has surveyed iCOM emission from the VLA1623−2417 protostellar cluster at 1.1 and 1.4 mm, at the spatial scale of 50 au. The main findings are summarized as follows:

(i) The spatial distribution of mm-size dust emission allows us to well detect VLA1623 A, B, and W. The binary companions A1 and A2 cannot be disentangled at the present angular resolution, but the circumbinary disc is clearly revealed. A proper motion of about 210 mas for both the A and B objects is clearly seen by comparing the present continuum image with that obtained at 0.9 mm in 2016 by Harris et al. (2018).

(ii) The present FAUST data set allows us to image, for the first time, methanol (CH_3OH) towards VLA1623−2417, using emission lines covering a wide rage of upper level excitation, E_u, from 45 to 537 K. Two spatially unresolved emission peaks are detected: (i) one associated with VLA1623 A and revealed by transitions up to E_u = 61 K, and (ii) another perfectly overlapping with VLA1623 B emitting up to E_u = 537 K.

(iii) From a non-LTE LVG analysis of the CH_3OH emission towards VLA1623 B, we obtain a size = 0.11–0.34 arcsec (14–45 au), and an A + E methanol column density N_{CH_3OH} = 10^{16}–10^{17} cm^{-2}. High kinetic temperatures and high volume densities are also required: $n_{H_2} \geq 10^8$ cm^{-3} and $T_{kin} \geq 170$ K. No LVG analysis can be done for VLA1623 A, given that it is detected only through lines in the E_u = 45–61 K range. An LTE RD analysis, however, provides $T_{rot} \leq 135$ K, and N_{tot} is ∼0.6–6 × 10^{14} cm^{-2}.

(iv) $HCOOCH_3$ emission is imaged towards VLA1623 B. Assuming the same gas conditions derived from methanol emission, we obtain a total column density (corrected for filling factor) N_{HCOOCH_3} = 1–2 × 10^{16} cm^{-2}. The $HCOOCH_3/CH_3OH$ abundance ratio, derived from the column densities, is ∼0.4, in agreement with the range of values obtained by previous interferometric measurements towards Class 0 and I hot corinos. Upper limits on the column densities of acetaldehyde, formamide, and dimethyl ether have been also derived.

(v) Methanol emission around VLA1623 B has a clear velocity gradient along the main axis of the disc, with a redshifted peak towards the NE and a blueshifted peak towards the SW. The CH_3OH spectra show two peaks (each ∼4–5 km s^{-1} broad), which are red- and blueshifted by ~6–7 km s^{-1} with respect to the systemic velocity. Assuming that CH_3OH traces the chemically enriched ring of the accretion disc close to the centrifugal barrier (as e.g. in the archetypical L1527 case), the bulk of the emission should be emitted at a radius of 33 au, a distance comparable with the size derived from LVG (14–45 au). Around VLA1623 A, CH_3OH is also rotating in the NE–SW direction but with the opposite sense in respect to VLA1623 B, and the emission is associated with A1. Thus, out of the coeval A1 + A2 binary, only A1 is associated with iCOMs and a hot corino, according to the present ALMA data. Observations at cm wavelengths are required to verify whether the detection of iCOM emission towards A2 is prevented by dust opacity. The spectra in this case are relatively narrow (~4 km s^{-1}). Assuming again a rotating ring, we derive a size of 12–24 au.

To conclude, thanks to the detection of CH_3OH and $HCOOCH_3$, VLA1623 B can be considered a new laboratory for studying astrochemistry around protostars. The inclination of the disc is 74°, close to edge-on. The data presented here are reminiscent of the first ALMA cycle observations towards the Orion HH212-mm protostellar disc at a spatial resolution of 50–100 au, revealing a velocity gradient of gas enriched in iCOMs around the disc. Once imaged in iCOMs at the 10 au scale, two rotating rings associated with the outer disc surface layers, above the optically thick equatorial plane, are observed around HH212-mm (Lee et al. 2019, and references therein). HH212-mm has thus become a rare but key region in which to investigate the chemical richness of the protostellar disc and its connection to either protostellar illumination or accretion shocks. VLA1623 B offers a second such region for examination, at a distance approximately three times closer than Orion.

ACKNOWLEDGEMENTS

We thank the referee P.T.P. Ho for the fruitful comments and suggestions. This project has received funding from: (1) the European Research Council (ERC) under the European Union's Horizon 2020 research and innovation programme, for the Project 'The Dawn of Organic Chemistry' (DOC), grant agreement no. 741002; (2) the PRIN-INAF 2016 The Cradle of Life – GENESIS-SKA (General Conditions in Early Planetary Systems for the rise of life with SKA); (3) a Grant-in-Aid from Japan Society for the Promotion of Science (KAKENHI: Nos. 18H05222, 20H05844, 20H05845); (4) the Spanish FEDER under project number ESP2017-86582-C4-1-R; (5) DGAPA, UNAM grants IN112417 and IN112820, and CONACyT, Mexico; (6) ANR of France under contract number ANR-16-CE31-0013; (7) the French National Research Agency in the framework of the Investissements d'Avenir programme (ANR-15-IDEX-02), through the funding of the 'Origin of Life' project of the Univ. Grenoble-Alpes, (8) the European Union's Horizon 2020 research and innovation programmes under projects 'Astro-Chemistry Origins' (ACO), Grant No. 811312; (9) the National Research Council Canada and an NSERC Dicovery Grant to DJ. This paper makes use of the following ALMA data: ADS/JAO.ALMA#2018.1.01205.L. ALMA is a partnership of ESO (representing its member states), NSF (USA) and NINS (Japan), together with NRC (Canada), MOST and ASIAA (Taiwan), and KASI (Republic of Korea), in cooperation with the Republic of Chile. The Joint ALMA Observatory is operated by ESO, AUI/NRAO, and NAOJ. The National Radio Astronomy Observatory is a facility of the National Science Foundation operated under cooperative agreement by Associated Universities, Inc.

DATA AVAILABILITY

The raw data will be available on the ALMA archive at the end of the proprietary period (ADS/JAO.ALMA#2018.1.01205.L).

REFERENCES

Andre P., Martin-Pintado J., Despois D., Montmerle T., 1990, A&A, 236, 180
André P., Ward-Thompson D., Barsony M., 1993, ApJ, 406, 122
Andre P., Ward-Thompson D., Barsony M., 2000, in Mannings V., Boss A. P., Russell S. S., eds, Protostars and Planets IV. Univ. Arizona Press, Tucson, AZ, p. 59
Belloche A. et al., 2020, A&A, 635, A198
Bianchi E. et al., 2020, MNRAS, 498, L87
Bouvier M., Ceccarelli C., López-Sepulcre A., Sakai N., Yamamoto S., Yang Y. L., 2022, ApJ, 929, 10
Caratti o Garatti A., Giannini T., Nisini B., Lorenzetti D., 2006, A&A, 449, 1077
Caselli P., Ceccarelli C., 2012, A&AR, 20, 56
Ceccarelli C., Maret S., Tielens A. G. G. M., Castets A., Caux E., 2003, A&A, 410, 587
Ceccarelli C., Caselli P., Herbst E., Tielens A. G. G. M., Caux E., 2007, in Reipurth B., Jewitt D., Keil K., eds, Protostars and Planets V. Univ. Arizona Press, Tucson, AZ, p. 47
Ceccarelli C. et al., 2017, ApJ, 850, 176
Codella C. et al., 2018, A&A, 617, A10
Codella C., Ceccarelli C., Chandler C., Sakai N., Yamamoto S., FAUST Team, 2021, Front. Astron. Space Sci., 8, 227
De Simone M. et al., 2017, A&A, 599, A121
De Simone M. et al., 2020, ApJ, 896, L3
Dubernet M.-L. et al., 2013, A&A, 553, A50
Endres C. P., Drouin B. J., Pearson J. C., Müller H. S. P., Lewen F., Schlemmer S., Giesen T. F., 2009, A&A, 504, 635
Fedele D. et al., 2018, A&A, 610, A24
Frank A. et al., 2014, in Beuther H., Klessen R. S., Dullemond C. P., Henning T., eds, Protostars and Planets VI. Univ. Arizona Press, Tucson, AZ, p. 451
Furuya R. S., Kitamura Y., Wootten A., Claussen M. J., Kawabe R., 2003, ApJS, 144, 71
Gagné J. et al., 2018, ApJ, 856, 23
Hara C. et al., 2021, ApJ, 912, 34
Harris R. J. et al., 2018, ApJ, 861, 91
Herbst E., van Dishoeck E. F., 2009, ARA&A, 47, 427
Hsieh C.-H., Lai S.-P., Cheong P.-I., Ko C.-L., Li Z.-Y., Murillo N. M., 2020, ApJ, 894, 23
Ilyushin V., Kryvda A., Alekseev E., 2009, J. Mol. Spectrosc., 255, 32
Jørgensen J. K. et al., 2016, A&A, 595, A117
Jørgensen J. K. et al., 2018, A&A, 620, A170
Kleiner I., Lovas F. J., Godefroid M., 1996, J. Phys. Chem. Ref. Data, 25, 1113
Lee C.-F., Ho P. T. P., Li Z.-Y., Hirano N., Zhang Q., Shang H., 2017a, Nat. Astron., 1, 0152
Lee C.-F., Li Z.-Y., Ho P. T. P., Hirano N., Zhang Q., Shang H., 2017b, Sci. Adv., 3, e1602935
Lee C.-F., Li Z.-Y., Ho P. T. P., Hirano N., Zhang Q., Shang H., 2017c, ApJ, 843, 27
Lee C.-F., Codella C., Li Z.-Y., Liu S.-Y., 2019, ApJ, 876, 63
Leous J. A., Feigelson E. D., Andre P., Montmerle T., 1991, ApJ, 379, 683
Lindberg J. E., Charnley S. B., Cordiner M. A., 2016, ApJ, 833, L14
Looney L. W., Mundy L. G., Welch W. J., 2000, ApJ, 529, 477
López-Sepulcre A. et al., 2017, A&A, 606, A121
McMullin J. P., Waters B., Schiebel D., Young W., Golap K., 2007, in Shaw R. A., Hill F., Bell D. J., eds, ASP Conf. Ser., vol. 376, Astronomical Data Analysis Software and Systems XVI. Astron. Soc. Pac., San Francisco, p. 127
Manigand S. et al., 2020, A&A, 635, A48
Maret S., Hily-Blant P., Pety J., Bardeau S., Reynier E., 2011, A&A, 526, A47

Motiyenko R. A., Tercero B., Cernicharo J., Margulès L., 2012, A&A, 548, A71
Müller H. S. P., Schlöder F., Stutzki J., Winnewisser G., 2005, J. Mol. Struct., 742, 215
Murillo N. M., Lai S.-P., 2013, ApJ, 764, L15
Murillo N. M., Lai S.-P., Bruderer S., Harsono D., van Dishoeck E. F., 2013, A&A, 560, A103
Murillo N. M., Harsono D., McClure M., Lai S. P., Hogerheijde M. R., 2018a, A&A, 615, L14
Murillo N. M., van Dishoeck E. F., van der Wiel M. H. D., Jørgensen J. K., Drozdovskaya M. N., Calcutt H., Harsono D., 2018b, A&A, 617, A120
Narayanan G., Logan D. W., 2006, ApJ, 647, 1170
Ohashi S. et al., 2022, ApJ, 927, 54
Oya Y., Sakai N., López-Sepulcre A., Watanabe Y., Ceccarelli C., Lefloch B., Favre C., Yamamoto S., 2016, ApJ, 824, 88
Pickett H. M., Poynter R. L., Cohen E. A., Delitsky M. L., Pearson J. C., Müller H. S. P., 1998, J. Quant. Spectrosc. Radiat. Transfer, 60, 883
Rabli D., Flower D. R., 2010, MNRAS, 406, 95
Sakai N. et al., 2014a, Nature, 507, 78
Sakai N. et al., 2014b, ApJ, 791, L38
Sakai N. et al., 2017, MNRAS, 467, L76
Santangelo G., Murillo N. M., Nisini B., Codella C., Bruderer S., Lai S. P., van Dishoeck E. F., 2015, A&A, 581, A91
Segura-Cox D. M. et al., 2020, Nature, 586, 228
Sheehan P. D., Eisner J. A., 2017, ApJ, 851, 45
Stahler S. W., Korycansky D. G., Brothers M. J., Touma J., 1994, ApJ, 431, 341
Taquet V., López-Sepulcre A., Ceccarelli C., Neri R., Kahane C., Charnley S. B., 2015, ApJ, 804, 81
Ward-Thompson D., Kirk J. M., Greaves J. S., André P., 2011, MNRAS, 415, 2812
Xu L.-H., Lovas F. J., 1997, J. Phys. Chem. Ref. Data, 26, 17
Xu L.-H. et al., 2008, J. Mol. Spectrosc., 251, 305
Yang Y.-L. et al., 2021, ApJ, 910, 20

[1] *INAF, Osservatorio Astrofisico di Arcetri, Largo E. Fermi 5, I-50125 Firenze, Italy*
[2] *Univ. Grenoble Alpes, CNRS, IPAG, F-38000 Grenoble, France*
[3] *Institut de Radioastronomie Millimétrique, F-38406 Saint-Martin d'Hères, France*
[4] *RIKEN Cluster for Pioneering Research, 2-1 Hirosawa, Wako-shi, Saitama 351-0198, Japan*
[5] *National Radio Astronomy Observatory, PO Box O, Socorro, NM 87801, USA*
[6] *Max-Planck-Institut für extraterrestrische Physik (MPE), Gießenbachstr. 1, D-85741 Garching, Germany*
[7] *Instituto de Radioastronomía y Astrofísica, Universidad Nacional Autónoma de México, A.P. 3-72 (Xangari), 8701 Morelia, Mexico*
[8] *Instituto de Astronomía, Universidad Nacional Autónoma de México, Ciudad Universitaria, A.P. 70-264, 04510 Cuidad de México, Mexico*
[9] *Dipartimento di Fisica e Astronomia, Università degli Studi di Firenze, via G. Sansone 1, I-50019 Sesto Fiorentino, Italy*
[10] *Departament de Física Quàntica i Astrofísica, Universitat de Barcelona (IEEC-UB), c/ Martí i Franqès 1, E-08028 Barcelona, Spain*
[11] *Center for Astrochemical Studies, Max-Planck-Institut für extraterrestrische Physik (MPE), Gießenbachstr. 1, D-85741 Garching, Germany*
[12] *CY Cergy Paris Université, Sorbonne Université, Observatoire de Paris, PSL University, CNRS, LERMA, F-95000 Cergy, France*
[13] *Department of Astronomy, Xiamen University, Zengcu'oan West Road, Xiamen 361005 China*
[14] *Center for Frontier Science, Chiba University, 1-33 Yayoi-cho, Inage-ku, Chiba 263-8522, Japan*
[15] *Department of Physics and Astronomy, University of Victoria, Elliott Building, 3800 Finnerty Road, Victoria, BC V8P 5C2, Canada*
[16] *NRC Herzberg Astronomy and Astrophysics, 5071 West Saanich Road, Victoria, BC V9E 2E7, Canada*
[17] *European Southern Observatory, Karl-Schwarzschild Str. 2, D-85748 Garching bei München, Germany*
[18] *Department of Astronomy, The University of Tokyo, 7-3-1 Hongo, Bunkyo-ku, Tokyo 113-0033, Japan*
[19] *Research Center for the Early Universe, The University of Tokyo, 7-3-1 Hongo, Bunkyo-ku, Tokyo 113-0033, Japan*

This paper has been typeset from a TEX/LATEX file prepared by the author.